Journal of Materials Chemistry A

Accepted Manuscript

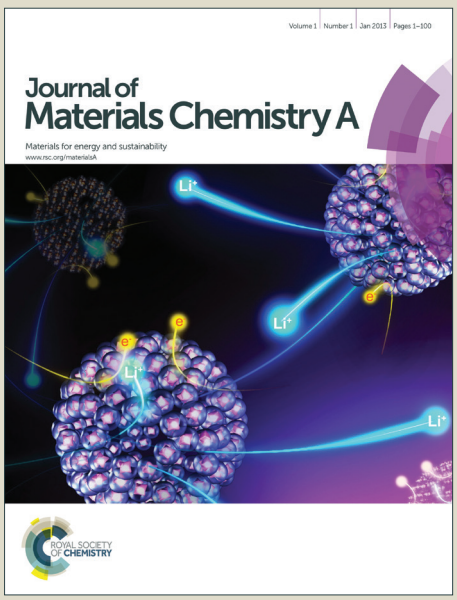

This is an *Accepted Manuscript*, which has been through the Royal Society of Chemistry peer review process and has been accepted for publication.

Accepted Manuscripts are published online shortly after acceptance, before technical editing, formatting and proof reading. Using this free service, authors can make their results available to the community, in citable form, before we publish the edited article. We will replace this *Accepted Manuscript* with the edited and formatted *Advance Article* as soon as it is available.

You can find more information about *Accepted Manuscripts* in the Information for Authors.

Please note that technical editing may introduce minor changes to the text and/or graphics, which may alter content. The journal's standard Terms & Conditions and the Ethical guidelines still apply. In no event shall the Royal Society of Chemistry be held responsible for any errors or omissions in this *Accepted Manuscript* or any consequences arising from the use of any information it contains.

ROYAL SOCIETY OF CHEMISTRY

www.rsc.org/materialsA

TOC

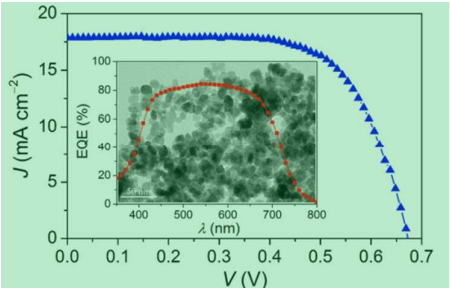

The dye-sensitized solar cell based on the Zn-doped SnO_2 nanocrystal photoanode has achieved a remarkable power conversion efficiency of 8.23%.

Journal of Materials Chemistry A Accepted Manuscript

Journal of Materials Chemistry A

Cite this: DOI: 10.1039/c0xx00000x

PAPER

www.rsc.org/xxxxxx

Zinc-doped SnO_2 nanocrystals as photoanode materials for highly efficient dye-sensitized solar cells

Xiaochao Li,[a] Qingjiang Yu,*[a] Cuiling Yu,*[b] Yuewu Huang,[a] Jinzhong Wang,*[a] Fengyun Guo,[a] Yong Zhang[a] and Liancheng Zhao[a]

Received (in XXX, XXX) Xth XXXXXXXXX 20XX, Accepted Xth XXXXXXXXX 20XX
DOI: 10.1039/b000000x

Zn-doped SnO_2 nanocrystals were successfully synthesized by a simple hydrothermal method. It is found that Zn doping into SnO_2 can induce a negative shift in the flat-band potential (V_{FB}) and increase the isoelectric point. As a result, the dye-sensitized solar cells (DSCs) based on Zn-doped SnO_2 nanocrystal photoanodes exhibit longer electron lifetimes and larger dye loading compared to the undoped SnO_2 based DSC. The overall power conversion efficiency (η) of the optimized Zn-doped SnO_2 based DSC reaches 4.18% and increases to 7.70% after the $TiCl_4$ treatment. More importantly, a remarkable η of 8.23% is achieved for the DSC based on a high-quality double-layer SnO_2 photoanode with the $TiCl_4$ treatment, to our best knowledge, which is so far the best reported efficiency for DSCs based on SnO_2 photoanodes.

1. Introduction

The growing demand for renewable energy sources has led to considerable development in many areas related to the research and manufacture of solar cells. Over the past two decades, dye-sensitized solar cells (DSCs) have attracted tremendous interest as a promising candidate for future green energy due to their low production cost and efficient photovoltaic performance.[1,2] As a crucial component of a DSC, the wide-gap semiconductor metal oxide plays two significant roles as a carrier for dye molecules and a transporter for the photoinjected electrons. Up to now, more than 12% power conversion efficiency has been reported for DSCs based on mesoporous TiO_2 nanocrystalline photoelectrodes.[3] Semiconductor metal oxides other than TiO_2, such as ZnO, SnO_2, and Nb_2O_5, have also been investigated as potential alternatives to TiO_2.[4-10] Among them, SnO_2 possesses a higher electron mobility (~100–200 $cm^2\ V^{-1}\ S^{-1}$)[11,12] than TiO_2 (<1 $cm^2\ V^{-1}\ S^{-1}$)[13], suggesting a faster diffusion transport of photoinjected electrons to a transparent conductive oxide current collector. Moreover, in comparison with TiO_2, SnO_2 have a larger band gap (3.6 eV), which would create fewer oxidative holes in the valence band, resulting in a low sensitivity of UV degradation and enhancement of the long-term stability of DSCs.[14]

However, the overall power conversion efficiencies (η) of SnO_2 based DSCs reported so far are much less than those of TiO_2 based DSCs. The inferior photovoltaic performances of DSCs with SnO_2 photoanodes are ascribed to the following: (1) a ~300 mV positive shift of the conduction band edge of SnO_2 in contrast to that of TiO_2, leading to a faster electron recombination of photoinjected electrons with the redox electrolyte and a lower of open circuit voltage (V_{oc});[15] (2) a lower isoelectric point (iep, at pH 4–5) than anatase TiO_2 (iep, at pH 6–7),[6] resulting in less adsorption of the dye with acidic carboxyl groups. To solve these issues, the general strategy has been carried out to enhance the photovoltaic performance of SnO_2 based DSCs by coating on SnO_2 photoanodes with a thin shell layer of semiconducting or isolating metal oxide, such as TiO_2, ZnO, MgO, and Al_2O_3.[6,14-21] It has been found that these thin shell layers can inhibit interfacial electron recombination and enhance the cell performance. Kuang et al. have achieved a highly efficient DSC with a power conversion efficiency of 6.8% based on the TiO_2 coated hierarchical SnO_2 octahedra.[22] Recently, Lee and coworker have reported that Zn doping in ordered mesoporous SnO_2 with a 2D hexagonal structure can tune the sub-band-edge surface states and improve the power conversion efficiency of ordered mesoporous SnO_2 based DSCs from 0.81 to 3.73%.[23] Shortly after that, Dou et al. have reported the power conversion efficiency for the DSC based on Zn-doped SnO_2 nanoflowers with high electron mobility can reach 3.0% and increase to 6.78% after TiO_2 coating.[24] Therefore, incorporating both the advantages of Zn-doped SnO_2 and TiO_2-coated SnO_2 is a good choice for improving the photovoltaic performance of SnO_2 based DSCs.

To date, the photoanodes are all comprised of nanocrystalline particles for high-efficiency DSCs due to their large surface area.[3,25-32] However, the DSCs based on Zn-doped SnO_2 nanocrystal phtotoanodes have not been investigated. Herein, we present the synthesis of Zn-doped SnO_2 nanocrystals by a simple hydrothermal method and their use as photoanodes in DSCs. It is found that the Zn doping can suppress the interfacial electron recombination and enhance dye-uptake capabilities. Consequently, the performance of the Zn-doped SnO_2 based DSC has a more than three-fold improvement compared to that of the

Journal of Materials Chemistry A Accepted Manuscript

undoped SnO_2 based DSC. Moreover, after the $TiCl_4$ post treatment of the photoanode, the Zn-doped SnO_2 based DSC exhibits an impressive power conversion efficiency of 7.70%. Finally, by employing a high-quality double-layer SnO_2 film with the $TiCl_4$ post treatment, the performance of the Zn-doped SnO_2 based DSC is further enhanced, achieving a remarkable efficiency of 8.23%. To the best of our knowledge, for the first time the DSC based on the SnO_2 photoanode exceeds the power conversion efficiency of 8%.

2. Experimental

2.1 Materials

Tin (IV) chloride pentahydrate ($SnCl_4{\cdot}5H_2O$), zinc acetate dihydrate ($Zn(CH_3COO)_2{\cdot}2H_2O$), ammonium hydroxide ($NH_4OH$), potassium stannate trihydrate ($K_2SnO_3{\cdot}3H_2O$), urea, titanium (IV) chloride ($TiCl_4$), ethanol and acetone were purchased from Sinopharm Chemical Reagent Co.,Ltd.. 1,3-dimethylimidazolium (DMII), lithium iodide (LiI), iodine (I_2), tert-butylpyridine (TBP), guanidinium thiocyanate (GNCS), acetonitrile, valeronitrile, tert-butanol, ethyl cellulose powders (nos. 46070 and 46080), α-terpineol, chenodeoxycholic acid were purchased from Sigma-Aldrich. The C106 dye was synthesized according to the literature method.[28]

2.2 Synthesis of undoped and Zn-doped SnO_2 nanocrystals

The undoped and Zn-doped SnO_2 nanocrystals were synthesized by a hydrothermal method. Typically, a mixture of 20 mL of deionized water containing 0.6 M of $SnCl_4{\cdot}5H_2O$ and a predetermined amount of $Zn(CH_3COO)_2{\cdot}2H_2O$ (0, 1, 2 and 4 at.% atom ratio to $SnCl_4{\cdot}5H_2O$) was slowly added to the ammonium hydroxide solution that was prepared by mixing 16 mL of NH_4OH with 24 mL of deionized water. The mixture was stirred for 2 h. The solution was transferred to a Teflon-lined stainless steel autoclave and heated at 200 °C for 12 h. After naturally cooling down to the room temperature, the white products were centrifugated, washed with deionized water and ethanol for several times, and finally dried at 60 °C.

2.3 Synthesis of SnO_2 spheres

The SnO_2 spheres were prepared using a modified hydrothermal method in an ethanol–water mixed solvent.[33] In a typical experiment, 19 mM $K_2SnO_3{\cdot}3H_2O$ and 0.1 M urea were added to a mixed solution of 12 mL ethanol and 18 mL deionized water. After mild magnetic stirring for 10 min, the solution was then transferred to a 50 mL Teflon-lined stainless steel autoclave and heated at 150 °C for 20 h. After naturally cooling down to the room temperature, the obtained products were centrifugated, washed with deionized water and ethanol for several times, and finally dried at 60 °C.

2.4 Electrode preparation and device fabrication

The typical preparation of the SnO_2 paste is according to the standard procedure for the DSC electrode fabrication.[34] The photoanode was made by screen printing the pastes onto a pre-cleaned fluorine-doped tin oxide (FTO) conducting glass (Nippon Sheet Glass, Solar, 4-mm-thick) with an active area of ~0.283 cm^2 and thickness of ~8.5 μm. The $TiCl_4$ treatment for the SnO_2 nanoparticle films was performed by immersing the SnO_2 photoanodes into a 40 mM $TiCl_4$ aqueous solution at 70 °C for 30 min. After that, the photoanodes were washed with deionized water and ethanol to remove residual $TiCl_4$, and then sintered at 500 °C in air for 30 min. Finally, the photoanodes was stained by immersing it into a dye solution containing C106 dye (150 μM) and chenodeoxycholic acid (2 mM) in the mixture of acetonitrile and tert-butanol (volume ratio: 1/1) for 20 h. The dye-coated SnO_2 electrode was subsequently washed with acetonitrile, and then assembled with a thermally platinized FTO positive electrode. The two active electrodes were separated with a 25-μm-thick Surlyn (DuPont) hot-melt gasket and sealed up by heating. The internal space was filled with electrolytes using a vacuum back filling system. The electrolyte-injecting hole on the counter electrode made with a sand-blasting drill, was sealed with a Surlyn sheet and a thin glass cover by heating. The electrolyte is composed of 1.0 M DMII, 50 mM LiI, 30 mM I_2, 1.0 M TBP, and 0.1 M GNCS in the 85/15 (volume ratio) mixture of acetonitrile and valeronitrile.

2.5 Characterization

X-ray power diffraction (XRD) analysis was conducted on a Rigaku D/max-2500 X-ray diffractometer with Cu Kα radiation (λ=1.5418 Å). Transmission electron microscope (TEM) and high-resolution TEM (HRTEM) observations were carried out with a JEOL JEM-2100 microscope operated at 200 KV. Field emission scanning electron microscopic (FESEM) images were performed on a JEOL JEM-6700F microscope operating at 5 KV. X-ray photoelectron spectroscopy (XPS) measurements were obtained from a PHI 5700 ESCA system. The Brunauer-Emmett-Teller (BET) surface area was determined by N_2 adsorption-desorption at 77 K using a BELSORP-max surface area analyzer. UV-vis absorbance spectra were recorded by Shinmadzu 3600 UV-vis Spectrophotometers. The dye loading capability was estimated by desorbing the dye into a ethanol–water mixed solution (volume ratio: 1/1) containing 0.1 M NaOH and subsequently measuring the absorption spectrum using a Shimadzu 3600 UV-vis spectrophotometer. The flat-band potential (V_{FB}) was calculated from the Mott-Schottky plots. The standard three-electrode configuration was used, with a platinum wire as the counter electrode and Ag/AgCl electrode as the reference.

2.6 Photovoltaic measurements

A Keithley 2400 source meter and a Zolix Omni-λ300 monochromator equipped with a 500 W xenon lamp were used to measure external quantum efficiency (EQE) spectra, with a wavelength sampling interval of 10 nm and a current sampling time of 2 s under the full computer control. A Hamamatsu S1337-1010BQ silicon diode used for EQE measurements was calibrated in National Institute of Metrology, China. A model LS1000-4S-AM1.5G-1000W solar simulator (Solar Light Company, USA) in combination with a metal mesh was employed to give an irradiance of 100 mW cm^{-2}. The light intensity was tested with a PMA2144 pyranometer and a calibrated PMA 2100 dose control system. Photocurrent density–voltage (J–V) characteristics were obtained by applying a bias potential to a testing cell and measuring photocurrent with a Keithley 2400 source meter under the full computer control. A metal mask with an aperture area of 0.158 cm^2 was covered on a testing cell during all measurements.

This journal is © The Royal Society of Chemistry [year]

Journal of Materials Chemistry A Accepted Manuscript

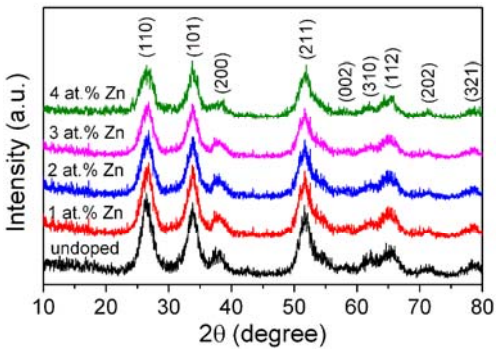

Fig. 1 XRD patterns of the undoped and Zn-doped SnO_2 nanoparticles.

An antireflection film (λ<380 nm, ARKTOP, ASAHI Glass) is adhered to the DSC photoanode during EQE and *J*–*V* measurements.

3. Results and discussion

The crystallographic structures of the undoped and Zn-doped SnO_2 nanoparticles were determined by XRD, as shown in Fig.1. All of the diffraction peaks can be indexed to tetragonal rutile SnO_2 (JCPDS, 41-1445). No diffraction peaks from other crystalline impurities were detected. This suggests that the dopants are well-dispersed and do not cause obvious variation in the SnO_2 lattice structure. However, the intensities of the diffraction peaks gradually reduce and the full-width at half-maximum increases with an increase in the Zn-doped content, which may be attributed to a decrease in the grain size upon incorporation of Zn into the SnO_2 crystal lattice.[36] Further, the morphology of the undoped and 2 at.% Zn-doped SnO_2 nanoparticles was characterized by TEM, as displayed in Fig. 2a and b. It is found that some larger particles obviously reduce in the 2 at.% Zn-doped SnO_2 nanoparticles compared to the undoped SnO_2 nanoparticles. The average grain size of the 2 at.% Zn-doped SnO_2 nanoparticles is ~15 nm. The representative HRTEM image of the 2 at.% Zn-doped SnO_2 nanoparticles is displayed in Fig. 2c. The clear lattice fringes in the HRTEM image indicate that these nanoparticles possess a single crystal structure. The inter-planar spacing is ~0.334 nm, corresponding to the (110) plane of rutile SnO_2.

To obtain more concrete proof for Zn doping in SnO_2, XPS measurements were conducted on the undoped and 2 at.% Zn-doped SnO_2 nanoparticles. Fig. 3a presents a comparison of the

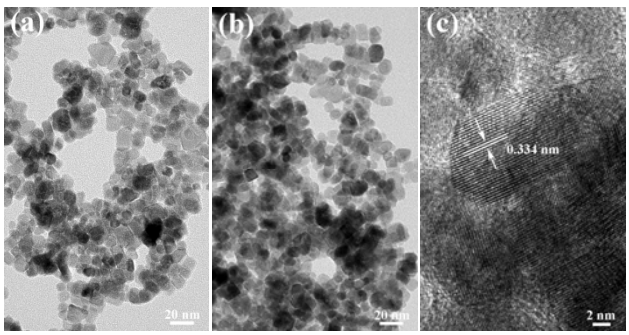

Fig. 2 (a) and (b) TEM images of undoped and 2 at.% Zn doped SnO_2 nanoparticles, respectively. (c) HRTEM image of 2 at.% Zn doped SnO_2 nanoparticles.

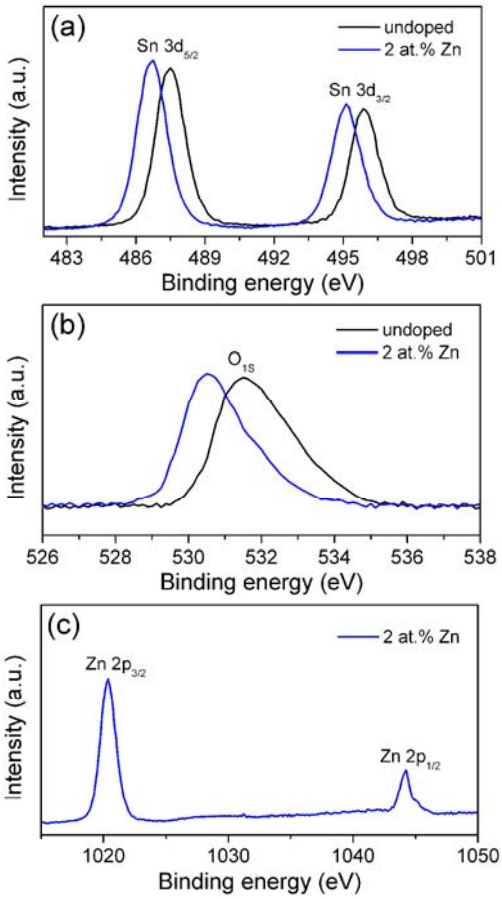

Fig. 3 XPS high-resolution spectra of undoped and Zn-doped SnO_2 nanoparticles: (a) Sn 3d, (b) O 1s, and (c) Zn 2p peaks.

Sn $3d_{5/2}$ and $3d_{3/2}$ transition peaks. Compared to the undoped SnO_2 nanoparticles, the binding energies of Sn $3d_{5/2}$ and $3d_{3/2}$ in the 2 at.% Zn-doped SnO_2 nanoparticles decrease from 487.4 to 486.6 eV and from 495.9 to 495.1 eV, respectively, which may be ascribed to oxide deficiency.[37] It is also found that the O 1s transition peak shifts from 531.1 to 529.8 eV upon Zn doping (Fig. 3b). The shoulder peak could be attributed to Sn-O-Zn coordination.[23] As shown in Fig. 3c, the binding energies of the Zn $2p_{3/2}$ and Zn $2p_{1/2}$ transition peaks are 1020.4 and 1044.3 eV, respectively, which confirms the presence of Zn in the doped SnO_2 nanoparticles.

The undoped and Zn-doped SnO_2 nanoparticles were using as photoanodes for DSCs. Fig. 4a shows the *J*–*V* characteristics of the cells based on the undoped and Zn-doped SnO_2 photoanodes under an irradiance of 100 mW cm^{-2} simulated AM1.5G sunlight and the detailed photovoltaic parameters are listed in Table 1. The short-circuit photocurrent density (J_{sc}), V_{oc} and fill factor (FF) of the cell with the undoped SnO_2 photoanode are 9.24 mA cm^{-2}, 335 mV and 0.428, respectively, generating a low η of 1.32%. When employing the Zn-doped SnO_2 photoanodes, the V_{oc} and J_{sc} values of the cells are significantly enhanced. A maximum η of 4.18% is obtained for the cell based on the 2 at.% Zn-doped SnO_2 photoanode.

For DSCs with a fixed redox electrolyte, it is widely recognized that the V_{oc} value is determined by the electron quasi-Fermi level in a given semiconductor material. To ascertain the

Journal of Materials Chemistry A Accepted Manuscript

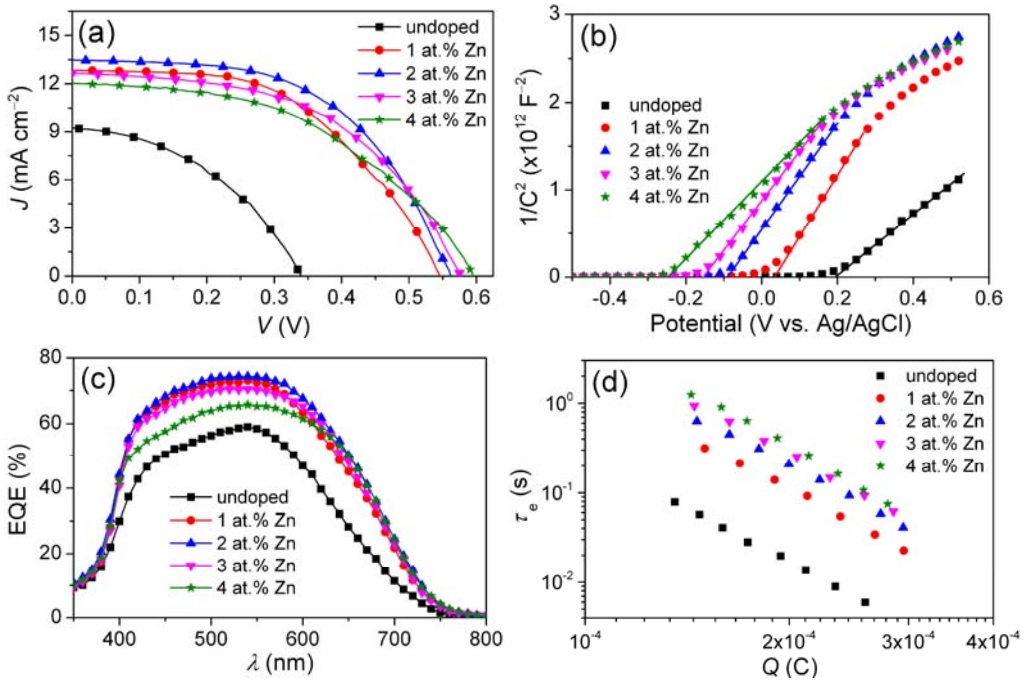

Fig. 4 (a) *J–V* characteristics of the undoped and Zn-doped SnO_2 based cells under an irradiance of 100 mW cm^{-2} simulated AM1.5G sunlight. (b) Mott-Schottky plots of the undoped and Zn-doped SnO_2 photoanodes. (c) EQE spectra of cells based on undoped and Zn-doped SnO_2 photoanodes. (d) Pots of lifetime of photoinjected electrons in the undoped and Zn-doped SnO_2 based cells as a function of charge.

influence of the Zn doping in SnO_2 on the band edge or quasi-Fermi level, the flat-band potentials of undoped and Zn-doped SnO_2 photoanodes were achieved from the Mott-Schottky analysis.[38-42] The V_{FB} can be determined by the following Mott-Schottky equation[43]

$$\frac{1}{C^2} = \left(\frac{2}{e\varepsilon\varepsilon_0 N_D A^2}\right)\left(V - V_{FB} - \frac{kT}{e}\right) \quad (1)$$

Where C is the differential capacitance of the space-charge region, e is the electron charge, ε is the dielectric constant of the semiconductor, ε_0 is the permittivity of vacuum, N_D denotes the donor density, A is the surface area of the electrode, V is the electrode potential, k is the Boltzman constant and T is the absolute temperature. The V_{FB} is the intercept extrapolating a straight line from the plot of the square of the space charge capacity against the applied potential. As shown in Fig. 4b, with increasing the Zn content, the V_{FB} shifts from 0.19 V for the undoped SnO_2 photoanode to –2.50 V for the 4 at.% Zn-doped SnO_2 photoanode. The negative movement may be caused through the passivation of the sub-band-edge surface states by doping Zn into the SnO_2 framework, leading to the upward shift of the quasi-Fermi level, which may interpret the enhanced V_{oc} witnessed in the corresponding cells.[23,41]

To comprehend the J_{sc} increment of the cells based on Zn-doped SnO_2 photoanodes, we measured the EQE spectra of these cells, as displayed Fig. 4c. The EQE data follow the same trend observed for the J_{sc} of the Zn-doped SnO_2 based cells. The EQE of the undoped SnO_2 based cell is about 59% at 540 nm. However, the incorporating Zn into SnO_2 causes an obvious increase in EQEs over the entire spectral range compared to the undoped SnO_2. The cell with the 2 at.% Zn-doped SnO_2 photoanode exhibits a maximum EQE of ~74% at 540 nm. However, when the Zn-doped content is more than 2 at.%, the cell shows a lower EQE compared to other Zn-doped SnO_2 based cells but is still higher than that of the undoped SnO_2 based cell.

Table 1. Detailed photovoltaic parameters of cells based on undoped and Zn-doped SnO_2 photoanodes.

	Zn doping (at.%)	Dye loading ($\times 10^{-7}$ mol cm^{-2})	V_{oc} (mV)	J_{sc} (mA cm^{-2})	FF	η (%)
no $TiCl_4$ treatment	0	3.94	335	9.24	0.428	1.32
	1	4.69	542	12.85	0.522	3.64
	2	5.18	560	13.48	0.554	4.18
	3	5.59	574	12.67	0.519	3.78
	4	5.95	591	12.04	0.484	3.44
$TiCl_4$ treatment	0	5.38	622	15.05	0.621	5.80
	1	6.03	665	16.48	0.669	7.43
	2	6.42	673	16.86	0.678	7.70
	3	6.77	682	16.29	0.671	7.45
	4	7.06	689	15.93	0.653	7.17

This journal is © The Royal Society of Chemistry [year]

Journal of Materials Chemistry A Accepted Manuscript

According to the above mentioned results, the negative movement of the V_{FB} may also be interpreted as a shift in the position of the conductor band edge of SnO_2 to higher potentials owing to Zn doping.[41] The higher conductor band edge may impede injection of photoelectrons and thereby degrades the EQE.

In contrast to the undoped SnO_2 based cell, the enhancement in the EQE and J_{sc} for the Zn-doped SnO_2 based cells may be intimately related to the dye loading and interfacial electron recombination.[44] The adsorbed amounts of dye molecules on different photoanodes were quantified from UV-visible absorption spectra. As shown in Table 1, the Zn doping can enhance the dye-uptake capabilities of SnO_2 photoanodes. With the increase of the Zn-doped content, the adsorbed amounts of dye molecules increase from 3.94×10^{-7} to 5.95×10^{-7} mol cm^{-2}, which can be explained by measured the isoelectric points of undoped and Zn-doped SnO_2 nanoparticles. As shown in Fig. S1, compared to the isoelectric point of the undoped SnO_2 nanoparticles, the present of Zn in SnO_2 nanoparticles increases the isoelectric point from 4.3 to 5.1, which favors the attachment of dye molecules with acidic carboxyl groups.[6] Accordingly, the Zn-doped SnO_2 based cells exhibit higher EQE and J_{sc} values.

To clarify the effect of the Zn doping in SnO_2 on the electron recombination process, we tested the dark current of the undoped and Zn-doped SnO_2 based cells. Although the dark current is not a direct measurement of the electron recombination, it is meaningful when the similar devices are compared. As displayed in Fig. S2, the dark current of the cell gradually decreases with increasing the Zn-doped content at a given potential, suggesting that the Zn doping in SnO_2 can restrain the electron recombination at the oxide/electrolyte interface. We further resorted to the transient photoelectric decay technique to measure the electron lifetime (τ_e) in the undoped and Zn-doped SnO_2 based cells. As depicted in Fig. 4d, the τ_e in the Zn-doped SnO_2 based cells is significantly higher than that in the undoped SnO_2 based cell at a certain extracted charge (Q) and increases with increasing the Zn-doped content, which is consistent with the trend observed in the dark current. The higher τ_e is attributed to the high electron mobility for the Zn-doped SnO_2 photoanodes.[24,45,46] It is well known that the τ_e in DSCs is the key quantity that determined the recombination dynamics in the solar cells.[47] The enhancement of the τ_e in the Zn-doped SnO_2 based cells shows the obvious inhibition of the electron recombination at the oxide/electrolyte interface. Since a low electron recombination rate is highly desirable to achieve a high charge-collection efficiency, which will also contribute to the higher EQE and J_{sc} as well as V_{oc}.

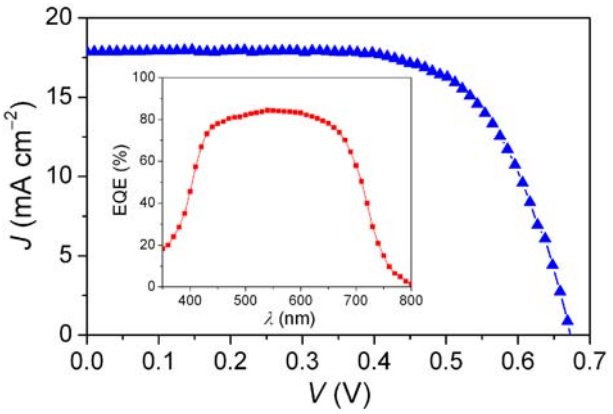

Fig. 5 J–V characteristics of the cells based on a double-layer film with the $TiCl_4$ treatment under an irradiance of 100 mW cm^{-2} simulated AM1.5G sunlight. The inset is its EQE spectrum

Table 2. Detailed photovoltaic parameters[a] of the cell based on a double-layer film with the $TiCl_4$ treatment under different incident light intensities.

P_{in} (mW cm^{-2})	V_{oc} (mV)	J_{sc} (mA cm^{-2})	FF	η (%)
12.16	581	2.34	0.777	8.69
23	618	4.31	0.745	8.63
50.62	644	9.27	0.714	8.42
100	670	17.87	0.687	8.23

[a] Lights at different intensities were obtained by attenuating the AM1.5G full sunlight with a set of neutral meshes. Incident power intensity: P_{in}.

In order to enhance their performance, the undoped and Zn-doped SnO_2 photoanodes were subjected to a treatment by a solution of $TiCl_4$. Fig. S3 shows the J–V characteristics of the undoped and Zn-doped SnO_2 based cells with the $TiCl_4$ treatment under an irradiance of 100 mW cm^{-2} simulated AM1.5G sunlight and the detailed photovoltaic parameters are also listed in Table 1. Compared to the cells without the $TiCl_4$ treatment, the photovoltaic parameters of the cells with the $TiCl_4$ treatment are significantly enhanced. The 2 at.% Zn-doped SnO_2 based cell with the $TiCl_4$ treatment achieves a power conversion efficiency of 7.70%. It is noteworthy that the 2 at.% Zn-doped SnO_2 based cell with the $TiCl_4$ treatment exhibits a higher efficiency compared to the DSCs based on SnO_2 photoanodes reported by other authors (Table S1), which is attributed to the high quality Zn-doped SnO_2 photoanode and C106 dye with high molar extinction coefficient. Moreover, it is found that the τ_e in the cells with the $TiCl_4$ treatment is longer at a certain extracted charge than that in the cells without the $TiCl_4$ treatment (Fig. S4), which is because the $TiCl_4$ treatment can improve the electronic connection of adjacent SnO_2 nanoparticles while slowing down the recombination processes,[48] resulting in the higher V_{oc}. After the $TiCl_4$ treatment, the J_{sc} enhancement of the cells is due to the increment of the dye loading (Table 1) as well as the suppression of the interfacial electron recombination.

We further employed a high-quality double-layer film via the $TiCl_4$ treatment, with a transparent layer based on 2 at.% Zn-doped SnO_2 nanocrystals and a scattering layer based on SnO_2 spheres (Fig. S5), to make a high-performance cell. As shown in Fig. 5, this cell has a J_{sc} of 17.87 mA cm^{-2}, a V_{oc} of 670 mV, and a FF of 0.687, yielding a remarkable efficiency of 8.23% under an irradiance of 100 mW cm^{-2} simulated AM1.5G sunlight. To our best knowledge, this is for the first time the DSC based on the SnO_2 photoanode exceeds the power conversion efficiency of 8%. The EQE spectrum of this high-efficiency cell is shown in the inset of Fig. 5. The EQEs exceed 80% in the region between 470 to 640 nm. In view that DSC is a very promising candidate for the conversion of weak light to electricity,[2] we also measured cell efficiencies by attenuating the AM1.5G full sunlight with a set of neutral metal meshes, and detailed cell parameters are collected in Table 2. At a light intensity of 12.16 mW cm^{-2}, this cell reaches an impressive efficiency of 8.69%.

Journal of Materials Chemistry A Accepted Manuscript

4. Conclusions

In summary, we have successfully synthesized Zn-doped SnO_2 nanocrystals under hydrothermal conditions and investigated their performance when applied as a photoanode material in DSCs. Zn doping into SnO_2 is observed to induce a negative shift in the flat-band potential and increase the isoelectric point. Consequently, the power conversion efficiency of 4.18% is achieved for the 2 at.% Zn-doped SnO_2 based DSC, which is a more than three-fold improvement in comparison with the undoped SnO_2 based DSC. The enhancement in performance is ascribed to improve electron lifetimes and dye-uptake capabilities. Moreover, after the $TiCl_4$ treatment of the photoanode, the 2 at.% Zn-doped SnO_2 based DSC exhibits an impressive power conversion efficiency of 7.70%. In conjunction with a high-quality double-layer SnO_2 film with the $TiCl_4$ treatment, the cell performance is further enhanced, reaching a remarkable efficiency of 8.23%. This is for the first time the DSC based on the SnO_2 photoanode exceeds the power conversion efficiency of 8%. Our work demonstrates that the Zn-doped SnO_2 nanocrystals coated with TiO_2 are a promising photoanode material for boosting the performance of DSCs.

Acknowledgements

This work was supported by the National 973 Program (Nos. 2011CBA00702 and 2015CB932204), the National 863 Project (No. 2013AA031502), the National Science and Technology Support Program (No. 2015BAI01B05), the National Natural Science Foundation of China (Nos. 51202046, 21203175, 51473158, 51125015, and 91233206), the Fundamental Research Funds for the Central Universities (Nos. HIT.NSRIF.2013006 and HIT.BRETIII.201403), and the China Postdoctoral Science Foundation (Nos. 2012M510087 and 2013T60366).

Notes and references

[a] *Department of Opto-electronic Information Science, School of Materials Science and Engineering, Harbin Institute of Technology, Harbin, 150001, China. Fax: +86 0451 86418328; Tel: +86 0451 86418745; E-mail: qingjiang.yu@hit.edu.cn; jinzhong_wang@hit.edu.cn*

[b] *Department of Physics, Harbin Institute of Technology, Harbin, 150001, China. Fax: +86 0451 86418328; Tel: +86 0451 86418745; E-mail: cuiling.yu@hit.edu.cn*

† Electronic Supplementary Information (ESI) available: [The pH-dependent zeta-potential of the undoped and Zn-doped SnO_2 nanoparticles; *J–V* characteristics of the undoped and Zn-doped SnO_2 based cells measured in the dark; *J–V* characteristics of the undoped and Zn-doped SnO_2 based cells with the $TiCl_4$ treatment; Comparison of the photovoltaic performance of the DSCs based on SnO_2 photoanodes with various morphologies; Pots of lifetime of photoinjected electrons in the DSCs based on undoped and Zn-doped SnO_2 photoanodes with $TiCl_4$ treatment as a function of charge; FESEM image of SnO_2 spheres.]. See DOI: 10.1039/b000000x/

1 B. O'Regan and M. Grätzel , *Nature*, 1991, **353**, 737–740.
2 M. Grätzel, *Acc. Chem. Res.*, 2009, **42**, 1788–1798.
3 A. Yella, H.-W. Lee, H. N. Tsao, C. Yi, A. K. Chandiran, M. K. Nazeeruddin, E. W.-G. Diau, C.-Y. Yeh, S. M. Zakeeruddin and M. Grätzel, *Science*, 2011, **334**, 629–634.
4 M. Law, L. E. Greene, J. C. Johnson, R. Saykally and P. Yang, *Nat. Mater.*, 2005, **4**, 455–459.
5 Q. Zhang, T. P. Chou, B. Russo, S. A. Jenekhe and G. Cao, *Angew. Chem. Int. Ed.*, 2008, **47**, 2402–2406.
6 A. Kay and M. Grätzel, *Chem. Mater.*, 2002, **14**, 2930–2935.
7 S. Chappel and A. Zaban, *Sol. Energy Mater. Sol. Cells*, 2002, **71**, 141–152.
8 P. Tiwana, P. Docampo, M. B. Johnston, H. J. Snaith and L. M. Herz, *ACS Nano*, 2011, **5**, 5158–5166.
9 K. Sayama, H. Sugihara and H. Arakawa, *Chem. Mater.*, 1998, 10, 3825–3832.
10 R. Katoh, A. Furube, T. Yoshihara, K. Hara, G. Fujihashi, S. Takano, S. Murata, H. Arakawa and M. Tachiya, *J. Phys. Chem. B*, 2004, **108**, 4818–4822.
11 Z. M. Arnold and J. P. Marton, *J. Electrochem. Soc.*, 1976, **123**, 299C–310C.
12 M. S. Arnold, P. Avouris, Z. W. Pan and Z. L. Wang, *J. Phys. Chem. B*, 2003, **107**, 659–663.
13 E. Hendry, M. Koeberg, B. O'Regan and M. Bonn, *Nano Lett.*, 2006, 6, 755–759.
14 M. K. I. Senevirathna, P. K. D. D. P. Pitigala, E. V. A. Premalal, K. Tennakone, G. R. A. Kumara and A. Konno, *Sol. Energy Mater. Sol. Cells*, 2007, **91**, 544–547.
15 A. N. M. Green, E. Palomares, S. A. Haque, J. M. Kroon and J. R. Durrant, *J. Phys. Chem. B*, 2005, **109**, 12525–12533.
16 S. Chappel. S.-G. Chen and A. Zaban, *Langmuir*, 2002, **18**, 3336–3342.
17 J. Qian, P. Liu, Y. Xiao, Y. Jiang, Y. Cao, X. Ai and H. Yang, *Adv. Mater.*, 2009, **21**, 3663–3667.
18 G. Shang, J. Wu, S. Tang, L. Liu and X. Zhang, *J. Phys. Chem. C*, 2013, **117**, 4345–4350.
19 U. V. Desai, C. Xu, J. Wu and D. Gao, *J. Phys. Chem. C*, 2013, **117**, 3232–3239.
20 M.-H. Kim and Y.-U. Kwon, *J. Phys. Chem. C*, 2011, **115**, 23120–23125.
21 C. Prasittichai and J. T. Hupp, *J. Phys. Chem. Lett.*, 2010, **1**, 1611–1615.
22 Y.-F. Wang, K.-N. Li, C.-L. Liang, Y.-F. Hou, C.-Y. Su and D.-B. Kuang, *J. Mater. Chem.*, 2012, **22**, 21495–21501.
23 E. Ramasamy and J. Lee, *Energy Environ. Sci.*, 2011, **4**, 2529–2536.
24 X. Dou, D. Sabba, N. Mathews, L. H. Wong, Y. M. Lam and S. Mhaisalkar, *Chem. Mater.*, 2011, **23**, 3938–3945.
25 M. K. Nazeeruddin, F. De Angelis, S. Fantacci, A. Selloni, G. Viscardi, P. Liska, S. Ito, B. Takeru and M. Grätzel, *J. Am. Chem. Soc.*, 2005, **127**, 16835–16847.
26 Y. Chiba, A. Islam, Y. Watanabe, R. Komiya, N. Koide and L. Han, *Jpn. J. Appl. Phys.*, 2006, **45**, L638–L640.
27 F. Gao, Y. Wang, D. Shi, J. Zhang, M. Wang, X. Jing, R. Humphry-Baker and P. Wang, *J. Am. Chem. Soc.*, 2008, **130**, 10720–10728.
28 Y. Cao, Y. Bai, Q. Yu, Y. Cheng, S. Liu, D. Shi, F. Gao and P. Wang, *J. Phys. Chem. C*, 2009, **113**, 6290–6297.
29 C.-Y. Chen, M. Wang, J.-Y. Li, N. Pootrakulchote, C. N. Alibabaei, J.-D. Decoppet, J.-H. Tsai, C. Grätzel, C.-G. Wu, S. M. Zakeeruddin and M. Grätzel, *ACS Nano*, 2009, **3**, 3103–3109.
30 Q. Yu, Y. Wang, Z. Yi, N. Zu, J. Zhang, M. Zhang and P. Wang, *ACS Nano*, 2010, **4**, 6032–6038.
31 L. Han, A. Islam, H. Chen, C. Malapaka, B. Chiranjeevi, S. Zhang, X. Yang and M. Yanagida, *Energy Environ. Sci.*, 2012, **5**, 6057–6060.
32 M. Zhang, Y. Wang, M. Xu, W. Ma, R. Li and P. Wang, *Energy Environ. Sci.*, 2013, **6**, 2944–2949.
33 X. W. Lou, Y. Wang, C. Yuan, J. Y. Lee and L. A. Archer, *Adv. Mater.*, 2006, **18**, 2325–2329.
34 P. Wang, S. M. Zakeeruddin, P. Comte, R. Charvet, R. Humphry-Baker and M. Grätzel, *J. Phys. Chem. B*, 2003, **107**, 14336–14341.
35 B. C. O'Regan, K. Bakker, J. Kroeze, H. Smit, P. Sommeling and J. R. Durrant, *J. Phys. Chem. B*, 2006, **110**,17155–17160.
36 V. Bilgin, S. Kose, F. Atay and I. Akyuz, *Mater. Lett.*, 2004, **58**, 3686–3693.
37 X. Liu, J. Iqbal, Z. Wu, B. He and R. Yu, *J. Phys. Chem. C*, 2010, **114**, 4790–4796.
38 M. Grätzel, *Nature*, 2001, **414**, 338–344.
39 D. F. Watson, A. Marton, A. M. Stux and G. J. Meyer, *J. Phys. Chem. B*, 2003, **107**, 10971–01973.
40 M. Radecha, M. Rekas, A. Trenczek-Zajac and K. Zakrzewska, *J. Power Sources*, 2008, **181**, 46–55.
41 X. Feng, K. Shankar, M. Paulose and G. A. Grimes, *Angew. Chem. Int. Ed.*, 2009, **48**, 8095–8098.

This journal is © The Royal Society of Chemistry [year]

Journal of Materials Chemistry A Accepted Manuscript

42 P. Xiang, X. Li, H. Wang, G. Liu, T. Shu, Z. Zhou, Z. Ku, Y. Rong, M. Xu, L. Liu, M. Hu, Y. Yang, W. Chen, T. Liu, M. Zhang and H. Han, *Nanoscale Res. Lett.*, 2011, **6**, 606-1–606-5.

43 R. van de Krol, A. Goossens and J. Schoonman, *J. Electronchem. Soc.*, 1997, **144**, 1723–1727.

44 H. J. Snaith and C. Ducati, *Nano Lett.*, 2010, **10**, 1259–1265.

45 Z. Li, Y. Zhou, T. Yu, J. Liu and Z. Zou, *CrystEngComm*, 2012, **14**, 6462–6468.

46 K.-P. Wang and H. Teng, *Phys. Chem. Chem. Phys.*, 2009, **11**, 9489–9496.

47 J. Bisquert, F. Fabregat-Santiago, I. Mora-Seró, G. Garcua-Belmonte and S. Biménez, *J. Phys. Chem. C*, 2009, **113**, 17278–17290.

48 L. Grinis, S. Kotlyar, S. Rühle, J. Grinblat and A. Zaban, *Adv. Funct. Mater.*, 2010, **20**, 282–228.

Journal of Materials Chemistry A Accepted Manuscript